Design of a High-Efficiency and -Gain Antenna Using Novel Low- Loss, Temperature-Stable Li 2 Ti 1 – x (Cu 1/3 Nb 2/3) x O 3 Microwave Dielectric Ceramics

Article *in* ACS Applied Materials & Interfaces · December 2020

DOI: 10.1021/acsami.0c18836

CITATIONS
40

READS
199

10 authors, including:

Di Zhou
Xi'an Jiaotong University
213 PUBLICATIONS **6,388** CITATIONS
SEE PROFILE

Chao Du
Xi'an Jiaotong University
17 PUBLICATIONS **215** CITATIONS
SEE PROFILE

Li-Xia Pang
Xi'an Technological University
109 PUBLICATIONS **4,059** CITATIONS
SEE PROFILE

ACS APPLIED MATERIALS & INTERFACES

www.acsami.org

Research Article

Design of a High-Efficiency and -Gain Antenna Using Novel Low-Loss, Temperature-Stable $Li_2Ti_{1-x}(Cu_{1/3}Nb_{2/3})_xO_3$ Microwave Dielectric Ceramics

Huan-Huan Guo, Mao-Sen Fu, Di Zhou,* Chao Du, Peng-Jian Wang, Li-Xia Pang, Wen-Feng Liu, Antonio Sergio Bezerra Sombra, and Jin-Zhan Su

Cite This: https://dx.doi.org/10.1021/acsami.0c18836

Read Online

ACCESS | Metrics & More | Article Recommendations | Supporting Information

ABSTRACT: Microwave dielectric ceramics are vital for filters, dielectric resonators, and dielectric antennas in the 5G era. It was found that the $(Cu_{1/3}Nb_{2/3})^{4+}$ substitution can effectively adjust the TCF (temperature coefficient of resonant frequency) of Li_2TiO_3 and simultaneously increase its $Q \times f$ (Q and f denote the quality factor and the resonant frequency, respectively) value. Notably, excellent microwave dielectric properties (ε_r (permittivity) ≈ 18.3, $Q \times f$ ≈ 77,840 GHz, and TCF ≈ +9.8 ppm/°C) were achieved in the $Li_2Ti_{0.8}(Cu_{1/3}Nb_{2/3})_{0.2}O_3$ ($LTCN_{0.2}$) ceramic sintered at 1140 °C. Additionally, the sintering temperature of $LTCN_{0.2}$ was reduced to 860 °C by the addition of 3 wt % H_3BO_3, exhibiting superior microwave dielectric properties (ε_r ≈ 21.0, $Q \times f$ ≈ 51,940 GHz, and TCF ≈ 1.4 ppm/°C) and being chemically compatible with silver. Moreover, $LTCN_{0.2}$ + 3 wt % H_3BO_3 ceramics were designed as a patch antenna and a dielectric resonator antenna, both of which showed high simulated radiation efficiencies (88.4 and 93%) and gains (4.1 and 4.03 dBi) at the center frequencies (2.49 and 10.19 GHz). The $LTCN_{0.2}$ + 3 wt % H_3BO_3 materials have promising future application for either 5G mobile communication devices and/or in low-temperature co-fired ceramic technology owing to their high Q, low sintering temperature, small density, and good temperature stability.

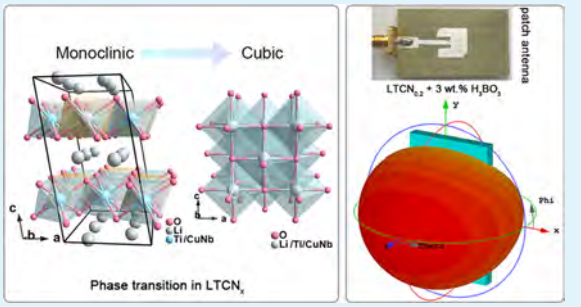

KEYWORDS: *microwave dielectric ceramics, temperature stabilities, antennas, phase transition, low-temperature sintering*

1. INTRODUCTION

In modern wireless communication, an important application field of microwave dielectric ceramic components is the mobile communication base station, while dielectric resonators, dielectric filters, duplexers, and multiplexers are the key components of communication base station RF units. 5G base stations will introduce communication technologies such as AAU (active antenna unit) RF unit integration and massive MIMO large-scale antenna arrays, prompting miniaturization and lightweight to become fundamental design requirements for communication base stations.[1−5] Therefore, high-performance microwave dielectric ceramics with low density have shown significant development potential in the 5G era due to the demand for lightweight.

The materials with a rock-salt-type structure are well known to the researchers.[6,7] Notably, among them, Li_2TiO_3 has attracted a considerable amount of attention due to its small density (~3.1 g/cm^3, which is lower than that of the commercial K20 microwave dielectric material: $0.95MgTiO_3$–$0.05CaTiO_3$ ≈ 3.7 g/cm^3.[8]), good performances, relatively low sintering temperature (~1230 °C), low cost, and abundant source features,[9,10] making it one of the most promising material candidates for 5G communication equipment. However, it still faces problems, such as a not high enough $Q \times f$ value (~23,600 GHz) and the large TCF (~+38.5 ppm/°C). It is known that the Q value and TCF are two crucial parameters for microwave dielectric ceramics. A higher Q value can achieve a better filtering function, and a near-zero TCF (temperature coefficient of resonant frequency) can achieve high reliability and stability of the microwave equipment. Hence, it is highly desirable to develop novel Li_2TiO_3-based microwave dielectric materials that possess both a high Q value and a near-zero TCF. For many titanate-based materials, oxygen vacancies are generated owing to the volatilization of oxygen during the sintering process in the air atmosphere. These positively charged oxygen vacancies can adsorb free electrons, causing Ti^{4+} to be reduced to Ti^{3+}. These Ti^{3+} ions are stable at room temperature, which is a cause of high dielectric loss.[11,12] It is noteworthy that Tian et al.[13,14]

Received: October 20, 2020
Accepted: December 12, 2020

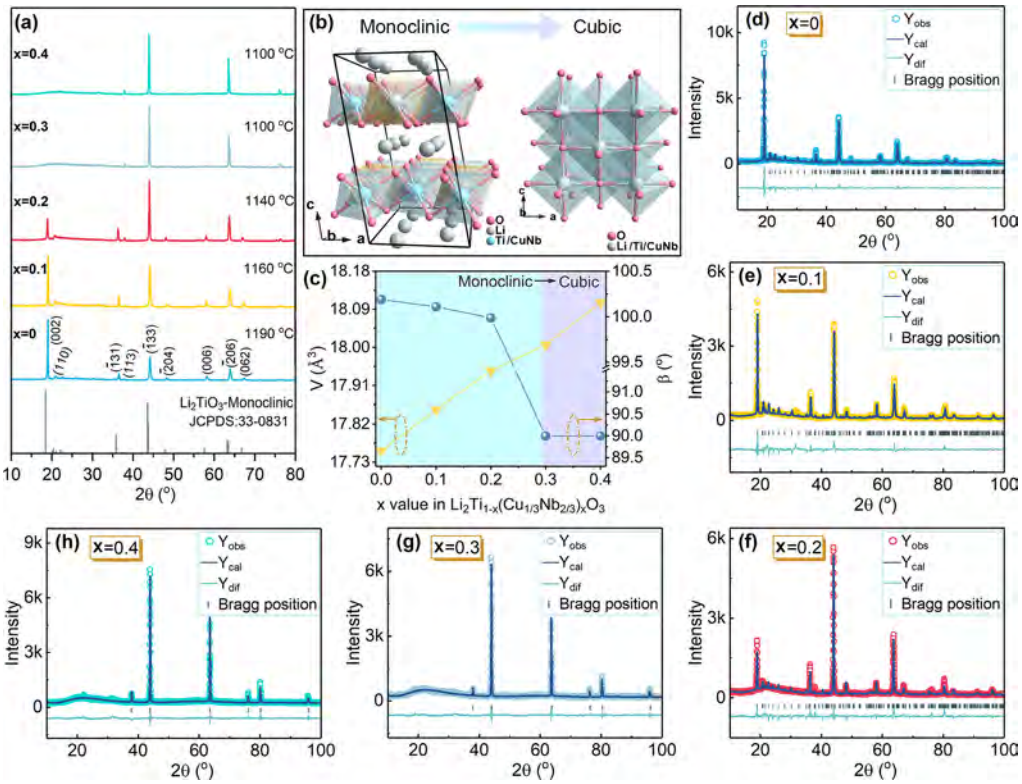

Figure 1. (a) XRD patterns of the $LTCN_x$ ($0 \le x \le 0.4$) specimens sintered at their optimum temperatures. (b) Schematic of two crystal structures in the $LTCN_x$ ($0 \le x \le 0.4$) system. (c) Variation of unit cell volume per oxygen ($\underline{V}$) and β angle with the x value. (d–h) Experimental and calculated XRD for $LTCN_x$ ($0 \le x \le 0.4$) specimens sintered at optimum temperatures.

reported that by introducing a high-valence ion at the B site of $BaTiO_3$ to form a complex ion with an average valence of +4, the oxygen vacancy content generated by electrostatic compensation would be greatly reduced, thereby reducing dielectric loss and improving the Q value of microwave dielectric ceramics. Moreover, this substitution method can also serve a role in regulating the TCF, which has an enlightening significance for our research. Based on aforementioned considerations, CuO as an acceptor dopant was first introduced to the Li_2TiO_3 ceramic in the present work. An adequate amount of CuO was also reported to be beneficial in reducing the sintering temperature.[15−17] In order to maintain the charge balance, Nb^{5+} was introduced to form $(Cu_{1/3}Nb_{2/3})^{4+}$ for replacing Ti^{4+}. Furthermore, the similar ionic radius between $(Cu_{1/3}Nb_{2/3})^{4+}$ (0.67 Å) and Ti^{4+} (0.605 Å)[18] would make the substitution process theoretically feasible.

In this paper, $Li_2Ti_{1-x}(Cu_{1/3}Nb_{2/3})_xO_3$ ($LTCN_x$) ($0 \le x \le 0.4$) specimens were fabricated by a conventional solid-state reaction. The effect of $(Cu_{13}Nb_{2/3})^{4+}$ substitution on the structure and performance of the Li_2TiO_3 ceramic has been studied in detail. Furthermore, to meet the application demands of integration, reducing the sintering temperature is also actively explored to adapt to low-temperature co-fired ceramic (LTCC) technology. LTCC is usually achieved by following three approaches: (i) chemical processing, (ii) novel low-temperature sintered materials, and (iii) adding a sintering agent. Among them, the last method is generally considered to be an effective, low-cost, and versatile method capable of reducing the sintering temperatures of ceramics.[19] It is worth mentioning that H_3BO_3 is a common and effective sintering aid with a low melting point.[20−24] Thus, it seems reasonable to believe that adding a H_3BO_3 additive can also effectively bring about a decrease in the sintering temperature of the $LTCN_x$ system. Effects of the H_3BO_3 content on crystalline structures, microstructures, densities, and microwave dielectric properties of the $LTCN_{0.2}$ ceramic (optimal performing sample) are investigated in this work. Meanwhile, the chemical compatibility of a H_3BO_3-doped $LTCN_{0.2}$ ceramic with silver was also studied. Moreover, the H_3BO_3-doped $LTCN_{0.2}$ ceramic was designed as a patch antenna and a dielectric resonator antenna using CST Microwave Studio software.

2. EXPERIMENTAL SECTION

Appropriate proportions of reagent-grade raw materials of Li_2CO_3 (99.99%), Nb_2O_5 (99.5%), TiO_2 (99.84%), and CuO (99%) were weighed based on the stoichiometric formulation $LTCN_x$ ($0 \le x \le 0.4$). These stoichiometric powders were ball milled using ZrO_2 beads with ethyl alcohol for 4 h. After drying, the homogeneous mixtures were calcined at 900 °C in air for 2 h. The resultant products were remilled for 4 h; after being dried and ground, the resultant products were mixed with PVA and then uniaxially compacted into cylinders with a height of approximately 4−5 mm. Specimens were sintered 2 h between 1080 and 1210 °C. In addition, to reduce the sintering temperature of $LTCN_{0.2}$, the calcined powders were re-milled with various amounts of H_3BO_3 in ethanol for 4 h. After being dried and sieved, the resultant products were mixed with PVA and then uniaxially compacted into cylinders with a height of approximately 4−5 mm. The H_3BO_3-doped $LTCN_{0.2}$ specimens were sintered at 840−1070 °C for 2 h.

The crystal structures were analyzed by an X-ray diffractometer (Rigaku D/MAX-2400). The XRD patterns were collected with a step size of 0.02° over the scan range of 10−100°. The microstructural observations were examined using transmission electron microscopy (JEM-2100) and scanning electron microscopy (Quanta F250). The mean grain sizes were calculated from each SEM image of specimens using Nano Measurer software. The far-IR spectra were collected on

https://dx.doi.org/10.1021/acsami.0c18836
ACS Appl. Mater. Interfaces XXXX, XXX, XXX−XXX

an infrared beamline at the Hefei National Synchrotron Radiation Laboratory. The Raman spectra were characterized from a Renishaw inVia Raman spectrometer. A microwave network analyzer (HP8720ES, Agilent) was used to characterize the microwave dielectric properties of ceramics and return loss (S_{11}) of the prototype antenna. The TCF test of 25−85 °C was conducted in a Delta 9023 temperature chamber, and the TCF test of −40 to +120 °C was conducted in a BPHJ-120C temperature chamber. The calculation of TCF is expressed by eq 1.

$$\mathrm{TCF}(\tau_f) = \frac{f_T - f_{T_0}}{f_{T_0} \times (T - T_0)} \times 10^6 \quad (1)$$

where T_0 denotes the onset temperature, T denotes the endset temperature, f_{T_0} denotes resonance frequency at T_0, and f_T denotes resonance frequency at T.

3. RESULT AND DISCUSSION

Figure 1a displays the XRD patterns for $LTCN_x$ ($0 \le x \le 0.4$) samples sintered at their optimum temperatures. The diffraction peaks of $x \le 0.2$ samples have been identified as the monoclinic Li_2TiO_3 structure with $C2/c$ symmetry (JCPDS #33-0831). Furthermore, the intensity of the diffraction peaks ($\bar{1}$ 33) and ($\bar{2}$06) increased with increasing x, while the intensity of the superlattice diffraction peak (002) gradually decreases and ultimately disappears at $x = 0.3$, suggesting that there is a phase transition from an ordered monoclinic to a disordered cubic phase. (The schematics of the crystal structure are displayed in Figure 1b). As a consequence, a continuous solid solution with a rock-salt-type structure is formed in the $LTCN_x$ ($0 \le x \le 0.4$) system, which is similar to the other reports.[7,25−27] To get a clear understanding of the correlation between the lattice parameters and the x value of $LTCN_x$ ceramics, refinements were carried out by GSAS software[28] based on the XRD patterns, which were collected from $LTCN_x$ ($0 \le x \le 0.4$) ceramic powders. Monoclinic ($C2/c$) and cubic ($Fm\bar{3}m$) Li_2TiO_3 were taken as starting models of $LTCN_x$ ($0 \le x \le 0.2$) and $LTCN_x$ ($0.3 \le x \le 0.4$) for Rietveld refinement, respectively.[29,30] The observed and calculated XRD patterns are displayed in Figure 1d−h. Furthermore, the refined lattice parameters are compiled in Table S1 (Supporting Information). The variation in unit cell volume per oxygen (V) with x is presented in Figure 1c, from which it could be concluded that the unit cell volume per oxygen is found to be increased with increasing x. This may be due to the fact that the ion radius of $(Cu_{1/3}Nb_{2/3})^{4+}$ (~0.67 Å) is larger than that of Ti^{4+} (~0.605 Å).[18] A similar phenomenon can be observed in the work reported by Chen et al.[25]

To extensively study the phase transformation, we have examined the SAED patterns and HRTEM imaging for $LTCN_x$ ($0.1 \le x \le 0.4$) ceramics. As displayed in Figure 2, the SAED patterns from the two compositions with the lower $(Cu_{1/3}Nb_{2/3})^{4+}$ amounts ($0.1 \le x \le 0.2$) could be well indexed based on the monoclinic structural phase, while the SAED patterns viewed along [001] for $LTCN_{0.3}$ and $LTCN_{0.4}$ could be analyzed based on the fcc rock-salt structural phase. Consistent with the results obtained from XRD, a phase transition from monoclinic to cubic could be observed from $LTCN_{0.2}$ to $LTCN_{0.3}$. Furthermore, extra superlattice reflections seen for $x \le 0.2$ indicate an ordered structure, whereas the diffuse scattering observed for $x \ge 0.3$ suggests a disordered structure, suggesting that an order−disorder phase transition also occurred around $x = 0.3$ for this system. Figure 2b,d,f,h shows the HRTEM images recorded along the

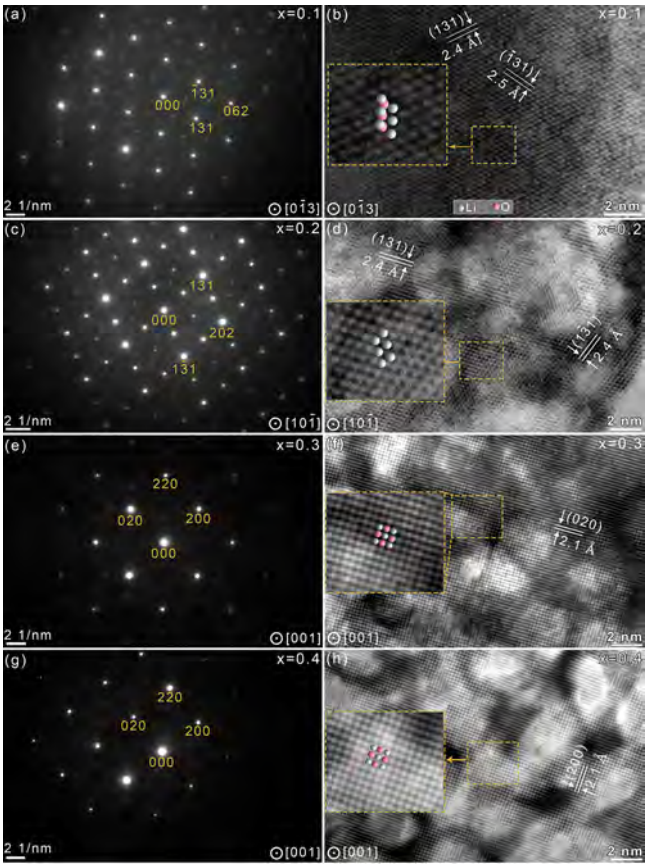

Figure 2. (a−h) SAED and HRTEM images of $LTCN_x$ ($0.1 \le x \le 0.4$) specimens taken along the [0 $\bar{1}$3], [10 $\bar{1}$], and [001] zone axes at room temperature, respectively. The structural models of the rock-salt unit cell were superimposed on the corresponding HRTEM micrographs.

corresponding zone axis as the SAED patterns. The crystal plane spacing in the SAED patterns is consistent with that in the HRTEM images, and it also agrees well with the crystal plane spacing calculated from the refined lattice parameters of $LTCN_x$ ($0.1 \le x \le 0.4$) samples. Moreover, structural models of the rock-salt unit cell are superimposed on the corresponding HRTEM micrographs. Raman spectroscopy is typically regarded as an efficient technique to identify the phase and short-range characteristics of the crystal materials.[31] The Raman spectrum of $LTCN_x$ ($0 \le x \le 0.4$) ceramics are displayed in Figure S1 (Supporting Information). The Raman spectra of $LTCN_x$ ($0 \le x \le 0.2$) specimens exhibit the similar spectral profiles to those of pure monoclinic Li_2TiO_3 owing to the forming of continuous solid solutions. In addition, as the x value increases, the bands less than 700 cm^{-1} show a certain degree of broadening, especially when $x \ge 0.3$. This is due to the reduction of the cation ordering degree, which further confirms that the $LTCN_x$ ($0 \le x \le 0.4$) system has an order−disorder phase transition. This also agrees well with XRD results. A new Raman peak at 806 cm^{-1} being in agreement with the symmetric vibration of the [NbO_6] octahedron is observed in $LTCN_x$ ($0.1 \le x \le 0.4$), which may be associated with the existence of a short-range order in the doped compositions.[26,32,33] In addition, the SEM images (Figure S2, Supporting Information) indicate that all the $LTCN_x$ ($0.1 \le x \le 0.4$) ceramics possess a micro-morphology with some pores,

https://dx.doi.org/10.1021/acsami.0c18836
ACS Appl. Mater. Interfaces XXXX, XXX, XXX−XXX

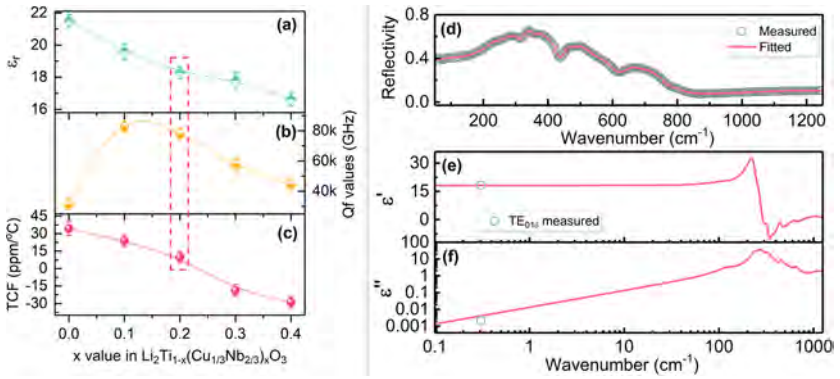

Figure 3. Variation in microwave dielectric properties (a) ε_r, (b) $Q \times f$, and (c) TCF with the x value for the LTCN$_x$ ($0 \le x \le 0.4$) specimens sintered at optimum temperatures. (d) Experimental and fitted infrared reflectance spectra and fitted (e) real and (f) imaginary parts of the complex dielectric constant of the LTCN$_{0.2}$ ceramic (blue circles represent experimental at microwave frequency).

resulting in a low relative density, possibly because of the evaporation of Li during sintering.

The variation in ε_r, $Q \times f$, and TCF with the x value for the LTCN$_x$ ($0 \le x \le 0.4$) specimens are displayed in Figure 3. It is observed that the ε_r decreased from 21.5 to 16.6 with the increase in x. Generally, it is considered that the permittivity of ceramics is affected by the ion polarizability of cations in the microwave frequency range. The ionic polarizabilities of various cations have been reported by Shannon.[34] It is supposed that an increase in the permittivity will be induced by the $(Cu_{1/3}Nb_{2/3})^{4+}$ substitution for Ti^{4+} because the ionic polarizability of the $(Cu_{1/3}Nb_{2/3})^{4+}$ ion ($\alpha_{average}$ = 3.35 Å^3, α_{Cu} = 2.11 Å^3, and α_{Nb} = 3.97 Å^3) is larger than that of Ti^{4+} (2.93 Å^3).[34] However, the ε_r of LTCN$_x$ is decreased in the range of x = 0−0.4. Thus, the variation in the permittivity of LTCN$_x$ is thought to depend significantly on its crystalline structure. As known from the periodic table of electronegativity (symbolized by X) using the Pauling scale, X_{Ti} = 1.54, X_{Cu} = 1.9, X_{Nb} = 1.59, and X_O = 3.44. Therefore, the electronegativity difference between Ti and O is $\Delta X_{(O-Ti)}$ = 1.9; the electronegativity difference between Cu and O is $\Delta X_{(O-Cu)}$ = 1.54; the electronegativity difference between Nb and O is $\Delta X_{(O-Nb)}$ = 1.85. The results show that both $\Delta X_{(O-Cu)}$ and $\Delta X_{(O-Nb)}$ are smaller than $\Delta X_{(O-Ti)}$. The smaller the difference in electronegativity between the two elements is, the stronger the covalency. Therefore, the covalency will increase after the $(Cu_{1/3}Nb_{2/3})^{4+}$ substitution for Ti^{4+}. Several previous studies have revealed that the increased covalency of the M−O bond in the [MO_6] octahedron by the ion substitution would lower the ε_r of ceramics,[35−38] for example, the Ta substitution for Nb in the [NbO_6] octahedron of $Mg_4(Nb_{2-x}Ta_x)O_9$ ceramics,[35] the Sb substitution for Nb in the [NbO_6] octahedron of $Mg_4(Nb_{2-x}Sb_x)O_9$ ceramics,[36] and the $(Zn_{1/3}Nb_{2/3})^{4+}$ substitution for Ti in the [TiO_6] octahedron of $Ba_3Ti_{4-x}(Zn_{1/3}Nb_{2/3})_xNb_4O_{21}$ ceramics.[37] Hence, the dielectric constant of LTCN$_x$ ($0 \le x \le 0.4$) ceramics decreased with an increase in x, which might be mainly ascribed to the fact that the covalency of the Ti−O bond is weaker than that of Cu−O and Nb−O bonds in an oxygen octahedron. As illustrated in Figure 3b, the $Q \times f$ was significantly increased by the minor substitution of $(Cu_{1/3}Nb_{2/3})^{4+}$ for Ti^{4+} in comparison to that of pure Li_2TiO_3, which was similar to many previously reported ceramic systems such as $Li_2Ti_{1-x}(Al_{1/2}Nb_{1/2})_xO_3$, $Li_2Ti_{1-x}(Zn_{1/3}Nb_{2/3})_xO_3$, Li_2TiO_3–MgO, and so on.[7,25,26,32,33] The dramatic increase in $Q \times f$ is potentially owed to the decrease in oxygen vacancy content. Since a high-valence ion (Nb^{5+}) is introduced into the B site of Li_2TiO_3 to form a complex ion with an average valence of +4, the oxygen vacancy content generated by electrostatic compensation would be greatly reduced, thereby reducing dielectric loss and improving the $Q \times f$ value of microwave dielectric materials. However, according to the results of XRD and TEM, an order−disorder phase transition occurs as x increases. Hence, the decrease in $Q \times f$ with further increasing $(Cu_{1/3}Nb_{2/3})^{4+}$ substitution could be attributed to the reduction of the ordering degree. As displayed in Figure 3c, the TCF value (measured from 25 to 85 °C) decreased from +34.3 to −28.8 ppm/°C with increased doping. The TCF values of perovskites were generally adjusted by changing the oxygen octahedral tilt angle. However, this seemed not to work in Li_2TiO_3 with a typical rock-salt crystal structure due to the fact that its oxygen octahedra were interconnected by edge sharing. Additionally, the TCF is known to be defined as follows:

$$\mathrm{TCF} = -\left(\alpha_l + \frac{1}{2}\tau_\varepsilon\right) \tag{2}$$

where α_l and τ_ε denote the thermal expansion coefficient and temperature coefficient of permittivity, respectively. The sign and magnitude of the TCF are known to be primarily determined by the τ_ε factor because the magnitude of α_l is usually constant and inconsequential in comparison to that of τ_ε in ceramics. Based on the macroscopic Clausius−Mossotti relationship, the τ_ε under the constant pressure conditions could be derived as follows:[39]

$$\tau_\varepsilon = \frac{1}{\varepsilon}\left(\frac{\partial \varepsilon}{\partial T}\right)_p = \frac{(\varepsilon - 1)(\varepsilon + 2)}{\varepsilon}(A + B + C) = \left(\varepsilon - \frac{2}{\varepsilon} + 1\right)(A + B + C) \tag{3}$$

$$A = -\frac{1}{3V}\left(\frac{\partial V}{\partial T}\right)_p,\ B = \frac{V}{\alpha_m}\left(\frac{\partial \alpha_m}{\partial V}\right)_T \cdot \frac{1}{3V}\left(\frac{\partial V}{\partial T}\right)_p,\ C = \frac{1}{3\alpha_m}\left(\frac{\partial \alpha_m}{\partial T}\right)_V \tag{4}$$

where α_m and V denote the dielectric polarizability and volume, respectively. It is considered that the terms of A and B, which are associated with volume expansion, have a close magnitude but with opposite signs, thereby the impact of terms

https://dx.doi.org/10.1021/acsami.0c18836
ACS Appl. Mater. Interfaces XXXX, XXX, XXX−XXX

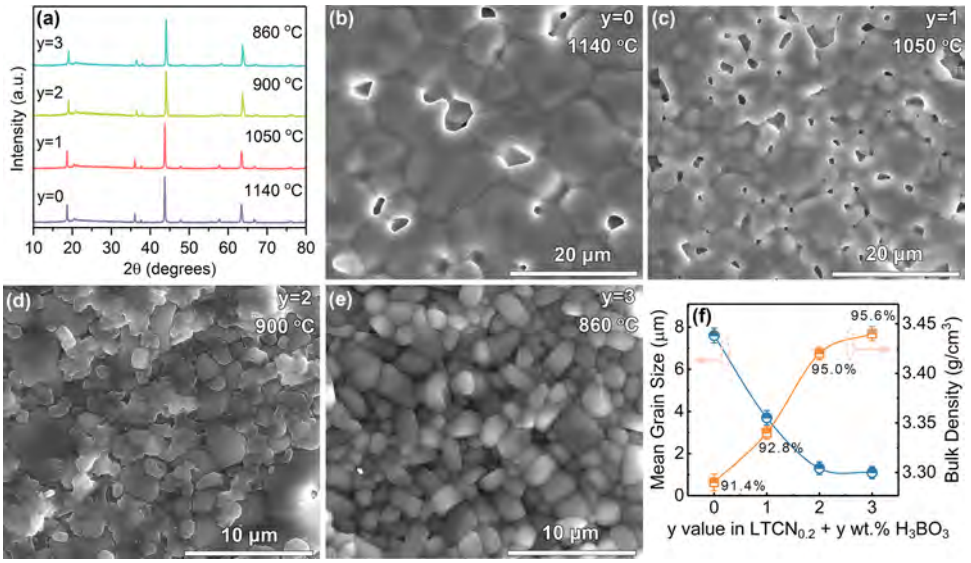

Figure 4. (a) XRD pattern of $LTCN_{0.2}$ + y wt % H_3BO_3 ($0 \le y \le 3$) specimens sintered at the optimum temperature. (b−e) SEM micrographs of $LTCN_{0.2}$ + y wt % H_3BO_3 ($0 \le y \le 3$) specimens. (f) Variation in mean grain size and density with y value for the $LTCN_{0.2}$ + y wt % H_3BO_3 ($0 \le y \le 3$) specimens sintered at optimum temperatures.

A and B on τ_ε is usually neglected.[39] Hence, the term C plays a dominating role in this system. Lee et al.[40] considered that the term C denotes the restoring force exerted on the ions and restoring force determined by the shape of the potential well, hence term C was related to structure and lattice parameters. Due to the fact that the unit cell volume has a robust association with lattice energy, τ_ε is proportional to the relative magnitude of the unit cell volume. Yoon et al. validated the presence of such a proportional relationship in the divalent metal tungstate.[41] The TCF and τ_ε are generally considered to have opposite signs, so it can be deduced that the TCF is inversely associated with the unit cell volume. As displayed in Figure 1c, the unit cell volume per oxygen (V) of $LTCN_x$ ($0 \le x \le 0.4$) specimens is positively related with x. Therefore, the TCF value would have a decrease with the increasing x. Notably, the TCF of Li_2TiO_3 could be successfully adjusted to around zero at x = 0.2, suggesting that the substitution of $(Cu_{1/3}Nb_{2/3})^{4+}$ at the B site of Li_2TiO_3 is a highly effective strategy for achieving temperature-stable microwave dielectric materials. Excellent performances could be achieved in the $LTCN_{0.2}$ specimen sintered at 1140 °C, with a ε_r of ∼18.3, a $Q \times f$ of ∼77,840 GHz, and a TCF of ∼+9.8 ppm/°C.

The infrared reflectance spectrum analysis was conducted based on the classical harmonic oscillator model (see eq 5 below) to further study the intrinsic microwave dielectric properties of the $LTCN_{0.2}$ ceramic.

$$\varepsilon^*(\omega) = \varepsilon(\infty) + \sum_{j=1}^{n} \frac{(z_j e)^2/m_j V_j \varepsilon_0}{\omega_{Tj}^2 - \omega^2 - j\gamma_j\omega} = \varepsilon(\infty) + \sum_{j=1}^{n} \frac{\omega_{Pj}^2}{\omega_{Tj}^2 - \omega^2 - j\gamma_j\omega} \quad (5)$$

For a detailed description of these terms, it can be seen in the previous literature.[42] The correlation between the complex reflectivity $R(\omega)$ and permittivity could be expressed as

$$R(\omega) = \left| \frac{1 - \sqrt{\varepsilon^*(\omega)}}{1 + \sqrt{\varepsilon^*(\omega)}} \right|^2 \quad (6)$$

Based on a good fitting, at a microwave frequency band ($\omega \ll \omega_{pj}$), thus, real and imaginary parts of permittivity could be readily obtained according to eq 7:

$$\varepsilon'(\omega) = \varepsilon(\infty) + \sum_{j=1}^{n} \frac{\omega_{Pj}^2}{\omega_{Tj}^2} = \varepsilon(\infty) + \sum_{j=1}^{n} \partial\varepsilon_j \quad (7)$$

$$\varepsilon''(\omega) = \omega \sum_{j=1}^{n} \frac{\partial\varepsilon_j\gamma_j}{\omega_{Tj}^2} \quad (8)$$

As displayed in Figure 3d, the room-temperature infrared reflection spectrum could be suitably fitted by using 12 Lorentz modes as tabulated in Table S2 (Supporting Information). Figure 3e,f presents the fitted complex dielectric spectrum, and the dielectric constant of the $LTCN_{0.2}$ ceramic was calculated to be 18.20. Furthermore, as seen in Figure 3e,f, the experimental values tested using the $TE_{01\delta}$ approach were remarkably close to the calculated permittivity and dielectric loss, implying that in the microwave frequency band, the dielectric polarization was caused primarily by phonon absorption in the infrared range.

LTCC has emerged as a critical technology for the demand of miniaturization, lightweight, and high integration of electronic devices, whereas the low-temperature co-fired ceramic materials are the most critical and fundamental issues for this technology. Hence, in order to be able to be co-fired with Ag for application to LTCC, how to lower the sintering temperature of the temperature-stable $LTCN_{0.2}$ ceramic to approximately 900 °C still requires further investigation. Generally, the engineering of additive is known to be a highly feasible and inexpensive approach to lower the sintering temperatures of ceramics.[19] Therefore, we investigated the impact of adding an H_3BO_3 additive on the sintering temperature of the $LTCN_{0.2}$ ceramic. The influence of sintering aids on the crystal structure was investigated in

https://dx.doi.org/10.1021/acsami.0c18836
ACS Appl. Mater. Interfaces XXXX, XXX, XXX−XXX

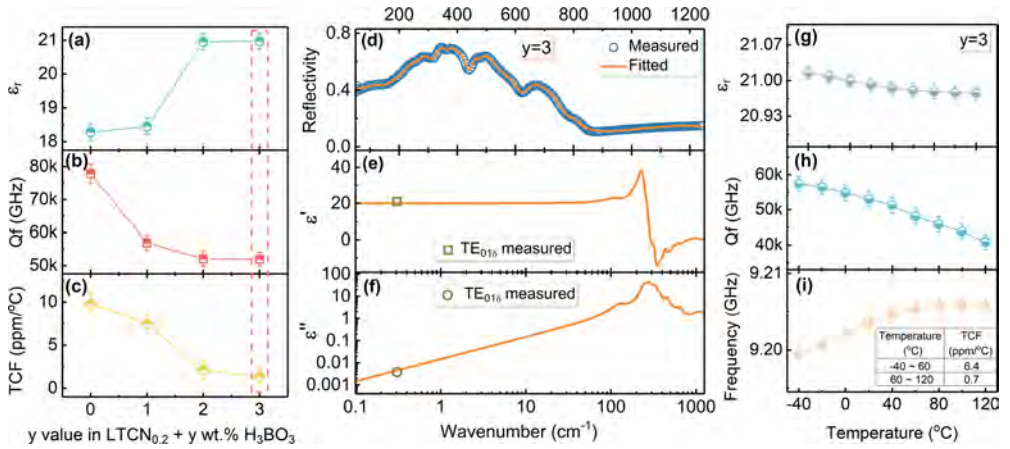

Figure 5. Variation in microwave dielectric properties (a) ε_r, (b) $Q \times f$, and (c) TCF with the y value for the $LTCN_{0.2}$ + y wt % H_3BO_3 ($0 \le y \le 3$) samples sintered at optimum temperatures. (d) Experimental and fitted infrared reflectance spectrum and the fitted (e) real and (f) imaginary parts of the complex dielectric constant of the $LTCN_{0.2}$ + 3 wt % H_3BO_3 ceramic (squares and circles represent experimental results in the microwave frequency band). (g) ε_r, (h) $Q \times f$, and (i) resonant frequencies of the $LTCN_{0.2}$ + 3 wt % H_3BO_3 ceramic with the changing of temperature.

detail. Figure 4a presents the XRD pattern of $LTCN_{0.2}$ + y wt % H_3BO_3 ($0 \le y \le 3$) specimens sintered at the optimal temperature. All the compounds showed a single $LTCN_{0.2}$ phase, and no secondary phases are observed. This suggested that the liquid phase of B_2O_3 is not crystallized in $LTCN_{0.2}$ ceramics and exists in an amorphous state after sintering. A similar phenomenon was also observed in relevant studies.[9,43,44] Additionally, the sintering temperature of $LTCN_{0.2}$ + y wt % H_3BO_3 ceramics was progressively lowered with increased doping, and the sintering temperature can be lowered to 860 °C when y = 3. The SEM micrographs of the $LTCN_{0.2}$ + y wt % H_3BO_3 ($0 \le y \le 3$) specimens sintered at the optimum temperature are displayed in Figure 4b−e. It was observed that the grain size showed a declining trend with the increasing amount of H_3BO_3. The average grain size of $LTCN_{0.2}$ + y wt % H_3BO_3 ($0 \le y \le 3$) ceramics decreased from 7.6 to 1.1 μm as demonstrated in Figure 4f, indicating that the H_3BO_3 significantly affects the growth behavior of grains. Due to the presence of the liquid phase reducing the driving force of the interface movement, the sintering additives facilitate the densification of ceramics but suppress the grain growth. Hence, the average crystallite sizes of H_3BO_3-doped samples were comparably smaller than those in the undoped $LTCN_{0.2}$ ceramic. A similar phenomenon was also observed in other studies.[45−48] As displayed in Figure 4f, the bulk density of $LTCN_{0.2}$ + y wt % H_3BO_3 ($0 \le y \le 3$) ceramics increased from 3.29 (relative density ≈ 91.4%) to 3.44 g/cm^3 (relative density ≈ 95.6%). In addition, it is clear that a small amount of pores exist in the microstructure of samples with $y \le 1$, while the samples with $y \ge 2$ exhibit a compact microstructure and almost no obvious pores. Based on the previous reports, the most rational explanation for the decrease in densification temperature is that the sintering procedure was assisted by liquid-phase transport across the grain boundaries.[49−51] The liquid phases of B_2O_3 contribute to the recrystallization and rearrangement of grain, leading the gases to readily diffuse away from the $LTCN_{0.2}$ ceramic, therefore forming a denser microstructure. All these results show that adding H_3BO_3 was a highly effective approach to improve the sintering capability of the $LTCN_{0.2}$ ceramic.

The variation in ε_r, $Q \times f$, and TCF with y for the $LTCN_{0.2}$ + y wt % H_3BO_3 ($0 \le y \le 3$) specimens are displayed in Figure 5a−c. The ε_r increased with increasing y and then reached a saturation value. The change of the ε_r value is primarily caused by the similar variation in density (Figure 4f). The greater the density of the ceramic body is, the more the number of dipoles per unit volume so the easier the ceramic can be polarized, which implies that the ceramic would have a higher ε_r value.[19,50] According to Figure 5b, the $Q \times f$ tended to decrease with the increment of H_3BO_3 content. On one hand, the decrease in the $Q \times f$ values for $LTCN_{0.2}$ + y wt % H_3BO_3 ($0 \le y \le 3$) ceramics was probably associated to the grain sizes as well as the grain shapes because the H_3BO_3 additive was effective in decreasing the grain sizes while simultaneously increasing the number of grain boundaries. However, the grain boundaries were perceived as a kind of surface defect in ceramics, which would bring much dielectric losses at the microwave regime. On the other hand, B_2O_3 should exist in the sintered products of $LTCN_{0.2}$ + y wt % H_3BO_3. Since the $Q \times f$ value of B_2O_3 is quite low,[52] the decreasing $Q \times f$ value of $LTCN_{0.2}$ + y wt % H_3BO_3 ceramics with y should be partially attributed to B_2O_3. As shown in Figure 5c, the TCF values (measured from 25 to 85 °C) of the samples decreased from +9.8 to +1.4 ppm/°C as the y values increased. Although the mechanism of the changes in TCF is not yet entirely clear at present, it seems reasonable to believe that the liquid phase of B_2O_3 is the cause of the changes of TCF. Similar phenomena have been reported in some other material systems after the addition of sintering aids.[22,23,46,47,53] Notably, the 3 wt % H_3BO_3-doped $LTCN_{0.2}$ ceramic sintered at 860 °C (which was 280 °C lower than that of undoped $LTCN_{0.2}$) exhibited a dense microstructure and superior performances of $\varepsilon_r \approx 21.0$, $Q \times f \approx 51{,}940$ GHz, and TCF ≈ +1.4 ppm/°C (25−85 °C).

To examine the intrinsic microwave dielectric properties of the $LTCN_{0.2}$ + 3 wt % H_3BO_3 ceramic further, the infrared reflectance spectrum analysis was conducted according to the classical harmonic oscillator model (see discussion above for the relative equations, eqs 5−8). As displayed in Figure 5d, the room temperature infrared reflection spectrum could be successfully fitted using 12 Lorentz modes as tabulated in Table S3 (Supporting Information). Figure 5e,f shows the fitted complex dielectric spectrum. The fitted complex microwave permittivity using eqs 7 and 8) are ∼20.1 and 0.0044, close to the experimental data, implying that in the

https://dx.doi.org/10.1021/acsami.0c18836
ACS Appl. Mater. Interfaces XXXX, XXX, XXX−XXX

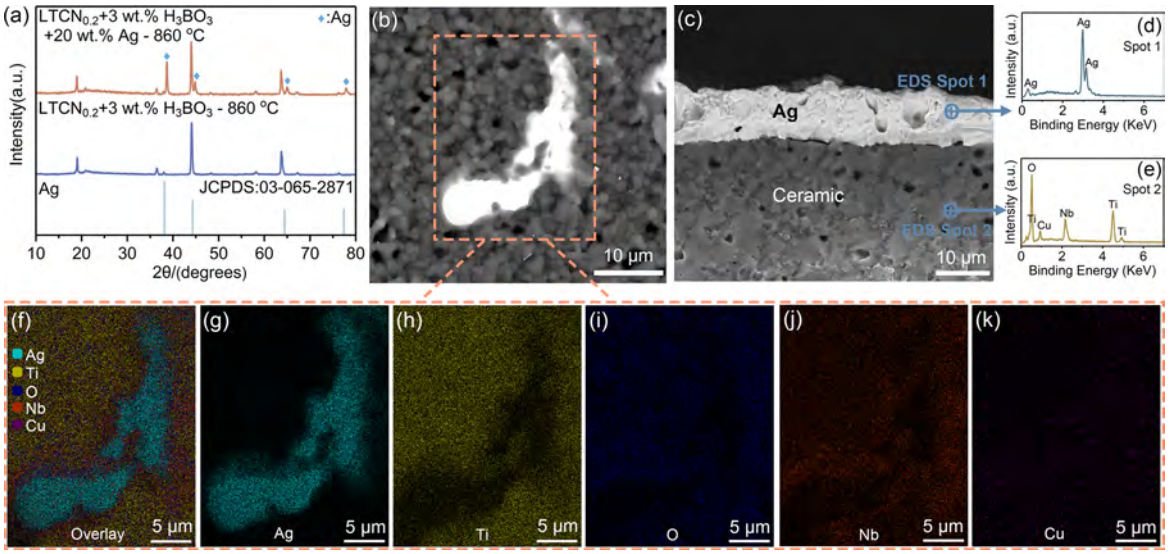

Figure 6. (a) XRD, (b) backscattered electron image, and (f–k) energy dispersive X-ray spectroscopy elemental mapping results of the $LTCN_{0.2}$ + 3 wt % H_3BO_3 ceramic co-fired with 20 wt % Ag powders at 860 °C. (c) Cross-sectional backscattered electron image and (d, e) EDS analysis of the silver paste coating on $LTCN_{0.2}$ + 3 wt % H_3BO_3 after co-firing at 860 °C for 2 h.

microwave frequency range, the dielectric polarization was induced primarily by phonon absorption in the infrared range.

Additionally, the communication rate has become faster with the advent of the 5G era, but meanwhile, the corresponding equipment is also facing some new problems. For example, the power consumption will increase obviously when the rate is increased, whereas a direct problem has brought to equipment components is that of the temperature will increase. Therefore, it puts forward a higher requirement for temperature stability of microwave dielectric ceramics. This means that the TCF (a crucial parameter to assess the temperature stability of microwave devices) needs to maintain a near-zero value over a wider temperature range. Currently, most studies involving TCF values have focused on the measured temperature range from 25 to 85 °C.[9,42,54−59] While in practical applications, the working temperature specifications of microwave devices such as ceramic dielectric filters are in the range of −40 to +85 °C, prompting us to explore the TCF over a wider range of temperatures. In view of this, the TCF of the $LTCN_{0.2}$ + 3 wt % H_3BO_3 ceramic over an ultra-wide temperature range from −40 to +120 °C was investigated. As displayed in Figure 5i, the resonant frequency of the $LTCN_{0.2}$ + 3 wt % H_3BO_3 ceramic initially increased and then remained relatively stable with increasing temperature. The result indicated that this ceramic has two different TCF values over the ultra-wide temperature range (−40 to +120 °C). It was calculated that the two TCF values at −40 to +60 °C and +60 to +120 °C were attributed to +6.4 and + 0.7 ppm/°C, respectively. Thus, it was obvious that the two TCF remain close to zero over an ultra-wide temperature range from −40 to +120 °C, showing an excellent temperature stability. As shown in Figure 5g, the permittivity of the $LTCN_{0.2}$ + 3 wt % H_3BO_3 ceramic remained relatively stable over the ultra-wide temperature range. In addition, the $Q \times f$ value exhibited a slightly declining trend as the temperature increases (Figure 5h). It shows that the dielectric properties also maintained relatively good stability in an ultra-wide temperature range. All these results indicate that this ceramic material has encouraging potential and holds great promise for future development as microwave equipment.

The sintering temperature (860 °C) of $LTCN_{0.2}$ + 3 wt % H_3BO_3 is significantly below the melting point of Ag. Although the low sintering temperature is necessary for LTCC, it is not sufficient because the chemical compatibility between the ceramic and Ag also plays an important role in LTCC applications. Thus, a further study to explore this compatibility is warranted. To verify if the silver reacts with the ceramic or not, mixtures of $LTCN_{0.2}$ + 3 wt % H_3BO_3 powders with 20 wt % Ag powders were co-fired at 860 °C and analyzed to detect chemical compatibility between them. XRD analysis confirmed that no new crystalline phases were formed after co-firing, as presented in Figure 6a. Moreover, two types of grains with different colors could be easily visible in the backscattered electron image (Figure 6b), which is more intuitive than XRD. According to the energy dispersive X-ray spectroscopy (EDS) elemental mapping results (Figure 6f–k), the dark- and light-colored grains indicate the phase of $LTCN_{0.2}$ and silver, respectively. Additionally, an alternative approach is to coat the silver paste on the unsintered $LTCN_{0.2}$ + 3 wt % H_3BO_3 sample and then co-fire at 860 °C for 2 h. Consequently, the chemical compatibility could also be judged by observing from the interface between Ag and the ceramic in the cross-sectional backscattered electron (BSE) image. The cross-sectional BSE image and the corresponding EDX analysis of the co-fired ceramic with Ag paste coating on $LTCN_{0.2}$ + 3 wt % H_3BO_3 are displayed in Figure 6c–e. Obviously, the interface of Ag and the $LTCN_{0.2}$ + 3 wt % H_3BO_3 ceramic after co-firing at 860 °C is clearly visible, revealing that no diffusion phenomena occur at the interface. In short, the $LTCN_{0.2}$ ceramic added by the 3 wt % H_3BO_3 can be well matched with silver. Overall, as a microwave dielectric material, the $LTCN_{0.2}$ + 3 wt % H_3BO_3 ceramic has superior performance, low sintering temperature, and good compatibility with Ag, and these characters enable them to be promising candidates for LTCC.

In recent decades, circularly polarized (CP) patch antennas have emerged as a matter of special interest to antenna designers because of their low profile, easy fabrication, and extensive use in wireless communication systems such as the global navigation satellite system (GNSS).[60,61] Furthermore, circular polarization is the most frequently applied in the

https://dx.doi.org/10.1021/acsami.0c18836
ACS Appl. Mater. Interfaces XXXX, XXX, XXX−XXX

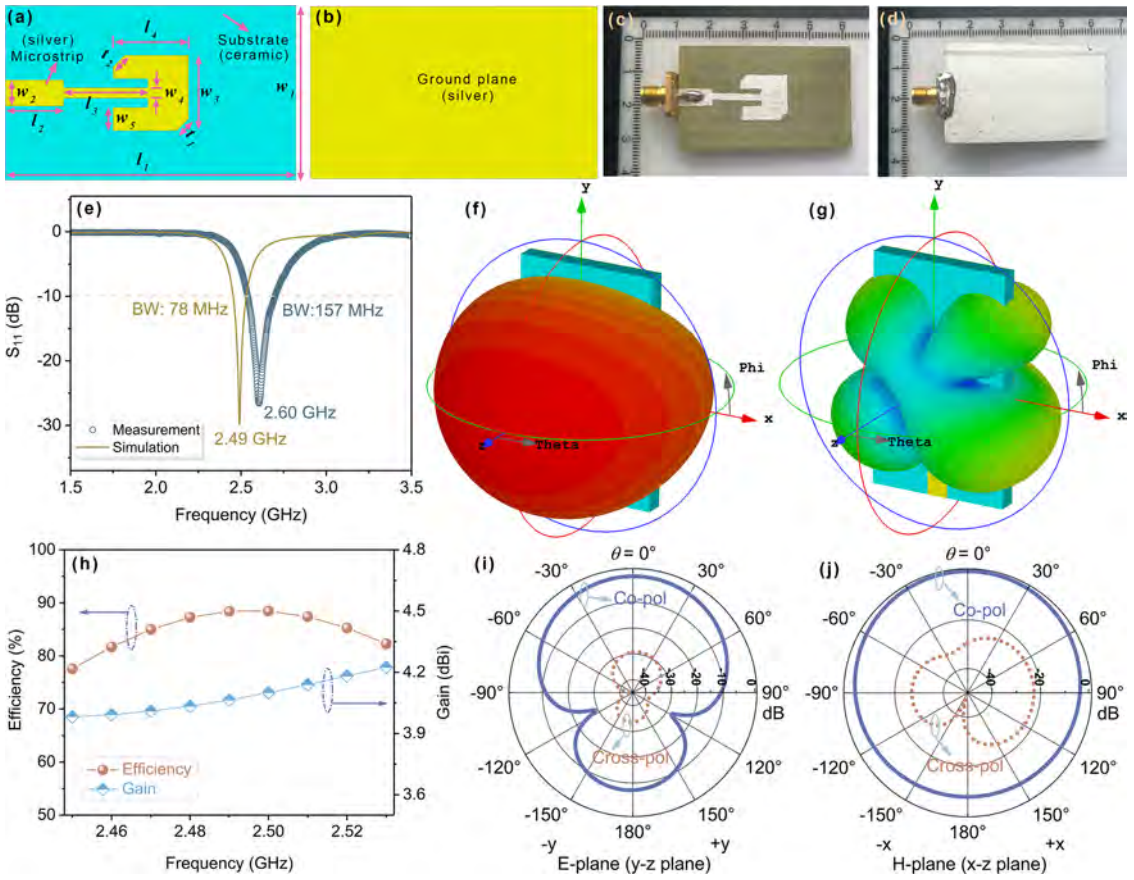

Figure 7. Geometry of the proposed antenna: (a) top view and (b) bottom view. Photograph of the fabricated antenna: (c) top view and (d) bottom view. (e) Simulated and experimental S_{11} of the proposed antenna. Simulated 3D radiation pattern of (f) co-polarized and (g) cross-polarized for the proposed antenna at 2.49 GHz. (h) Simulated antenna radiation efficiencies and gains of the proposed antenna as a function of frequency. Simulated radiation patterns of (i) *E* and (j) *H* planes.

GNSS with the performance of decreasing polarization mismatch and enhancing system sensitivity.[62] As an important member of the GNSS, the BeiDou Navigation Satellite System (BDS) was already available for the Asia-Pacific region to offer positioning and timing services.[63] Therefore, we specifically choose $LTCN_{0.2}$ + 3 wt % H_3BO_3 for the dielectric substrate to design a CP patch antenna for BeiDou applications. The geometry of the proposed antenna is displayed in Figure 7a,b. The designed antenna is fed by a microstrip transmission line along a non-radiating edge. In addition, to realize circularly polarized radiation from a rectangular microstrip antenna with a single driving point, we removed a pair of corners from the microstrip antenna to create the orthogonal modes. The proposed antenna configuration is numerically studied and optimized with the CST Microwave Studio. The optimum parameters of the proposed antenna are listed in Table S4 (Supporting Information). A prototype of the proposed antenna was manufactured according to the optimal simulation, and the photographs are shown in Figure 7c,d. The simulated and experimental S_{11} of the proposed antenna with various frequencies are displayed in Figure 7e. The simulated S_{11} result showed the antenna centers at 2.49 GHz with an impedance bandwidth of 78 MHz, which can cover the operating frequency of the BDS in China with a working band of 2491.75 ± 15 MHz.[61] It is observed that the measured S_{11} result shifted toward the higher frequency (center at 2.60 GHz) while maintaining similar responses. The minor difference between measurements and simulations could be owed to the fabrication tolerance (the antenna is totally made by hand), and the dielectric constant of the substrates may not be entirely uniform.[63−66] The simulated radiation patterns of the proposed antenna at 2.49 GHz are displayed in Figure 7f,g,i,j. Both the *E* and *H* planes for right-hand circular polarization (RHCP) at 2.49 GHz were nearly omnidirectional radiation patterns. Furthermore, the co-polarized fields were stronger than that of the cross-polarized ones by more than 20 dB in the boresight direction (θ = 0°). Figure 7h shows the simulated radiation efficiencies and gains of the proposed antenna. As can be seen, the radiation efficiencies are higher than 77.6% in the bandwidth (88.4% at the center frequency), and the gain is around 4.1 dBi at the center frequency. The results indicate that the proposed antenna may find important applications in the BDS.

The dielectric resonator antennas (DRAs) have already been widely investigated over the last several decades because of their appealing characteristics such as easy excitation, low cost, and relatively wide bandwidth.[67,68] The $LTCN_{0.2}$ + 3 wt % H_3BO_3 ceramics possess superior microwave properties with high *Q* and high temperature stability. To validate the performance of the fabricated materials, a DRA was designed and manufactured. Figure 8a,b shows different views of the prototype of the proposed DRA along with its dimensions in millimeter. The microwave substrate was made of Rogers 5880 with a thickness of 1.5 mm. A 50 Ω microstrip feedline was printed on the bottom layer of the substrate to energize the slot. The DRA was simulated using the CST software. Figure

https://dx.doi.org/10.1021/acsami.0c18836
ACS Appl. Mater. Interfaces XXXX, XXX, XXX−XXX

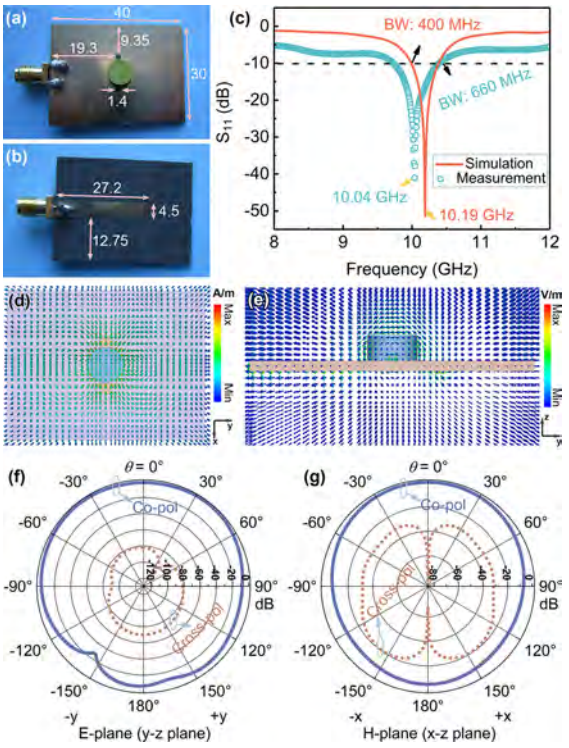

Figure 8. Configuration of the slot-coupled cylindrical DRA (unit: millimeter): (a) top view and (b) bottom view. (c) Simulated and experimental S_{11} of the proposed DRA with the changing of frequency. Simulated (d) magnetic and (e) electric field distributions of the proposed DRA at 10.19 GHz. Simulated radiation pattern of the DRA at 10.19 GHz: (f) *E* plane and (g) *H* plane.

8c displays the simulated and experimental S_{11} of the DRA. The experimental and simulated resonance frequencies of the DRA are given by 10.04 and 10.19 GHz, respectively. For the bandwidth, the experimental and simulation values are 660 and 400 MHz (S_{11} < −10 dB), respectively. Thus, the central frequency of the simulation exhibits an extremely great agreement with the experimental result. With the intention of revealing the physical mechanism of the proposed DRA, the simulated magnetic- and electric-field distributions were examined at a frequency of 10.19 GHz (as presented in Figure 8d,e). It can be observed from Figure 8d that the magnetic field distribution displays an ellipse-like shape, which is caused by the electromagnetic wave oscillation between the microstrip line and the ground plane along the *z* axis.[69] In addition, Figure 8e shows the simulated electric field distribution, from which it can be seen that the displacement current in the proposed DRA was horizontal. It shows that the slot-coupled feeding method can excite the $HEM_{11\delta}$ resonance mode. The simulated radiation patterns are displayed in Figure 8f,g. As shown, the cross-polarized fields are weaker than the co-polarized ones by more than 20 dB in the boresight direction (θ = 0°), indicating that the cylindrical DRA has a good polarization purity. In addition, the DRA has high radiation efficiency (93%) at the resonance frequency (10.19 GHz) and exhibits around 4.03 dBi maximum gain.

4. CONCLUSIONS

The phase transition and microwave dielectric properties of $LTCN_x$ ($0 \le x \le 0.4$) were intensively researched. A phase transition from the monoclinic phase to the cubic phase is found to happen at x = 0.3. The substitution of $(Cu_{1/3}Nb_{2/3})^{4+}$ for Ti^{4+} proved to be effective in adjusting the TCF to near zero while improving the $Q \times f$ value. Remarkably, superior microwave dielectric properties with $\varepsilon_r \approx 18.3$, $Q \times f \approx 77{,}840$ GHz, and TCF ≈ +9.8 ppm/°C were achieved in the $LTCN_{0.2}$ ceramic sintered at 1140 °C. In addition, the 3 wt % H_3BO_3-doped $LTCN_{0.2}$ ceramic provides a number of favorable features such as low sintering temperature (~860 °C), small density (~3.44 g/cm^3), and good chemical compatibility with silver together with superior performances of $\varepsilon_r \approx 21.0$, $Q \times f \approx 51{,}940$ GHz, and TCF ≈ +1.4 ppm/°C, which endow it broad application prospect in either 5G mobile communication devices and/or in LTCC technology. Furthermore, both the prototype dielectric resonator antenna and patch antenna designed by $LTCN_{0.2}$ + 3 wt % H_3BO_3 materials show good performances. The DRA provides high simulated radiation efficiency (~93%) and gain (~4.03 dBi) at the center frequency (~10.19 GHz). The patch antenna provides high simulated radiation efficiency (~88.4%) and gain (~4.1 dBi) at the center frequency (~2.49 GHz), and it exhibits light weight and low cost, which might find potential applications in the BDS.

■ ASSOCIATED CONTENT

Supporting Information

The Supporting Information is available free of charge at https://pubs.acs.org/doi/10.1021/acsami.0c18836.

Refined lattice parameters of $LTCN_x$ ($0 \le x \le 0.4$) ceramics (Table S1), Raman spectra of $LTCN_x$ ($0 \le x \le 0.4$) ceramics (Figure S1), SEM images and densities of the $LTCN_x$ ($0 \le x \le 0.4$) specimens (Figure S2), phonon parameters achieved from the fitting of the infrared reflectivity spectra of the $LTCN_{0.2}$ specimen (Table S2), phonon parameters achieved from the fitting of the infrared reflectivity spectra of the $LTCN_{0.2}$ + 3 wt % H_3BO_3 ceramic (Table S3), and optimized parameters of the proposed patch antenna (Table S4) (PDF)

■ AUTHOR INFORMATION

Corresponding Author

Di Zhou − *Key Laboratory of Multifunctional Materials and Structures, Ministry of Education, School of Electronic Science and Engineering, Xi'an Jiaotong University, Xi'an 710049, Shaanxi, China;* orcid.org/0000-0001-7411-4658; Email: zhoudi1220@gmail.com

Authors

Huan-Huan Guo − *Key Laboratory of Multifunctional Materials and Structures, Ministry of Education, School of Electronic Science and Engineering, Xi'an Jiaotong University, Xi'an 710049, Shaanxi, China*

Mao-Sen Fu − *Shaanxi Materials Analysis and Research Center, School of Materials Science and Engineering, Northwestern Polytechnical University, Xi'an, Shaanxi 710072, China*

Chao Du − *Key Laboratory of Multifunctional Materials and Structures, Ministry of Education, School of Electronic Science and Engineering, Xi'an Jiaotong University, Xi'an 710049, Shaanxi, China*

Peng-Jian Wang − *Key Laboratory of Multifunctional Materials and Structures, Ministry of Education, School of*

https://dx.doi.org/10.1021/acsami.0c18836
ACS Appl. Mater. Interfaces XXXX, XXX, XXX−XXX

Electronic Science and Engineering, Xi'an Jiaotong University, Xi'an 710049, Shaanxi, China

Li-Xia Pang − *Micro-optoelectronic Systems Laboratories, Xi'an Technological University, Xi'an, Shaanxi 710032, China*

Wen-Feng Liu − *State Key Laboratory of Electrical Insulation and Power Equipment, Xi'an Jiaotong University, Xi'an, Shaanxi 710049, China*

Antonio Sergio Bezerra Sombra − *Telecommunication Engineering Department, Federal University of Ceará (UFC), Fortaleza, Ceará 60755-640, Brazil; Telecommunication and Materials Science and Engineering of Laboratory (LOCEM), Physics Department, Federal University of Ceará (UFC), Pici Campus, Fortaleza, Ceará 60455-760, Brazil*

Jin-Zhan Su − *International Research Centre for Renewable Energy, State Key Laboratory of Multiphase Flow in Power Engineering, Xi'an Jiaotong University, Xi'an, Shaanxi 710049, China;* orcid.org/0000-0003-1757-4900

Complete contact information is available at: https://pubs.acs.org/10.1021/acsami.0c18836

Notes

The authors declare no competing financial interest.

■ ACKNOWLEDGMENTS

This study was supported by the National Key Research and Development Program of China (grant 2017YFB0406301), the State Key Laboratory of Electrical Insulation and Power Equipment (grant EIPE19210), the Fundamental Research Funds for the Central University, and the 111 Project of China (B14040). The authors thank the administrators in the IR beamline workstation (BL01B) of the National Synchrotron Radiation Laboratory (NSRL) for their help in the IR measurement and fitting. The SEM and TEM works were done at the International Center for Dielectric Research (ICDR), Xi'an Jiaotong University, Xi'an, China, and the authors thank Ms. Yan-Zhu Dai and Mr. Chuan-Sheng Ma for their help in using SEM and TEM.

■ REFERENCES

(1) Elijah, O.; Leow, C. Y.; Rahman, T. A.; Nunoo, S.; Iliya, S. Z. A Comprehensive Survey of Pilot Contamination in Massive MIMO—5G System. *IEEE Commun. Surv. Tutorials* **2016**, *18*, 905−923.

(2) Xiao, K.; Gong, L.; Kadoch, M. Opportunistic Multicast NOMA with Security Concerns in a 5G Massive MIMO System. *IEEE Commun. Mag.* **2018**, *56*, 91−95.

(3) Krishna, M. B.; Lloret Mauri, J. *Advances in Mobile Computing and Communications: Perspectives and Emerging Trends in 5G Networks*; CRC Press: Boca Raton, 2016, 1−425.

(4) Khan, I.; Zafar, M.; Jan, M.; Lloret, J.; Basheri, M.; Singh, D. Spectral and Energy Efficient Low-Overhead Uplink and Downlink Channel Estimation for 5G Massive MIMO Systems. *Entropy* **2018**, *20*, 92.

(5) Liu, F.; Guo, J.; Zhao, L.; Shen, X.; Yin, Y. A Meta-Surface Decoupling Method for Two Linear Polarized Antenna Array in Sub-6 GHz Base Station Applications. *IEEE Access* **2019**, *7*, 2759−2768.

(6) Mather, G. C.; Dussarrat, C.; Etourneau, J.; West, A. R. A Review of Cation-Ordered Rock Salt Superstructure Oxides. *J. Mater. Chem.* **2000**, *10*, 2219−2230.

(7) Bian, J. J.; Dong, Y. F. New High Q Microwave Dielectric Ceramics with Rock Salt Structures: $(1-x)Li_2TiO_3+xMgO$ System ($0 \le x \le 0.5$). *J. Eur. Ceram. Soc.* **2010**, *30*, 325−330.

(8) Xiaojing, Y.; Shihua, D.; Xiaobing, L.; Bo, Y.; Xiuling, Y.; Tianxiu, S. The Structure and Properties of $0.95MgTiO_3-0.05CaTiO_3$ Ceramics Co-doped with $ZnO-ZrO_2$. *Ceram. Int.* **2012**, *38*, S61−S64.

(9) Pang, L. X.; Zhou, D. Microwave Dielectric Properties of Low-Firing Li_2MO_3 (M=Ti, Zr, Sn) Ceramics with B_2O_3-CuO Addition. *J. Am. Ceram. Soc.* **2010**, *93*, 3614−3617.

(10) Tsuchiya, K.; Kawamura, H.; Casadio, S.; Alvani, C. Effects of Gelation and Sintering Conditions on Granulation of Li_2TiO_3 Pebbles From Li−Ti Complex Solution. *Fusion Eng. Des.* **2005**, *75-79*, 877−880.

(11) Wolfram, G.; Göbel, H. E. Existence Range, Structural and Dielectric Properties of $Zr_xTi_ySn_zO_4$ Ceramics (x+y+z=2). *Mater. Res. Bull.* **1981**, *16*, 1455−1463.

(12) Negas, T.; Yeager, G.; Bell, S.; Coats, N.; Minis, I. $BaTi_4O_9$/$Ba_2Ti_9O_{20}$-Based Ceramics Resurrected for Modern Microwave Applications. *Am. Ceram. Soc. Bull.* **1993**, *72*, 80−89.

(13) Tian, C.; Yue, Z.; Meng, S.; Zhou, Y.; Alford, N. Structures and Microwave Dielectric Properties of $Ba[Ti_{1-x}(Co_{0.5}W_{0.5})_x]O_3$ (x = 0.40-0.90) Perovskite Ceramics. *J. Am. Ceram. Soc.* **2012**, *95*, 1645−1650.

(14) Tian, C.; Yue, Z.; Zhou, Y.; Li, L. Crystal Structures and Microwave Dielectric Properties of Zn,W Co-substituted $BaTiO_3$ Perovskite Ceramics. *J. Solid State Chem.* **2013**, *197*, 242−247.

(15) Park, H. Y.; Ahn, C. W.; Cho, K. H.; Nahm, S.; Lee, H. G.; Kang, H. W.; Kim, D. H.; Park, K. S. Low-Temperature Sintering and Piezoelectric Properties of CuO-Added $0.95(Na_{0.5}K_{0.5})NbO_3$-$0.05BaTiO_3$ Ceramics. *J. Am. Ceram. Soc.* **2007**, *90*, 4066−4069.

(16) Park, S. J.; Park, H. Y.; Cho, K. H.; Nahm, S.; Lee, H. G.; Kim, D. H.; Choi, B. H. Effect of CuO on the Sintering Temperature and Piezoelectric Properties of Lead-Free $0.95(Na_{0.5}K_{0.5})NbO_3-0.05CaTiO_3$ Ceramics. *Mater. Res. Bull.* **2008**, *43*, 3580−3586.

(17) Nam, C. H.; Park, H. Y.; Seo, I. T.; Choi, J. H.; Nahm, S.; Lee, H. G. Effect of CuO on the Sintering Temperature and Piezoelectric Properties of MnO_2-doped $0.75Pb(Zr_{0.47}Ti_{0.53})O_3-0.25Pb(Zn_{1/3}Nb_{2/3})O_3$ Ceramics. *J. Alloys Compd.* **2011**, *509*, 3686−3689.

(18) Shannon, R. D. Revised Effective Ionic Radii and Systematic Studies of Interatomic Distances in Halides and Chalcogenides. *Acta Crystallogr.* **1976**, *32*, 751−767.

(19) Liang, J.; Lu, W. Z.; Wu, J. M.; Guan, J. G. Microwave Dielectric Properties of Li_2TiO_3 Ceramics Sintered at Low Temperatures. *Mater. Sci. Eng., B* **2011**, *176*, 99−102.

(20) Bi, J. X.; Xing, C. F.; Yang, C. H.; Wu, H. T.; Jiang, X. S. Low Temperature Sintering and Microwave Dielectric Properties of $MnZrNb_2O_8$ Ceramics with H_3BO_3 Addition. *J. Alloys Compd.* **2016**, *676*, 9−14.

(21) Zhang, P.; Hua, Y.; Xia, W.; Li, L. Effect of H_3BO_3 on the Low Temperature Sintering and Microwave Dielectric Properties of $Li_2ZnTi_3O_8$ Ceramics. *J. Alloys Compd.* **2012**, *534*, 9−12.

(22) Bi, J. X.; Xing, C. F.; Jiang, X. S.; Yang, C. H.; Wu, H. T. Low Temperature Sintering and Microwave Dielectric Properties of $CoZrNb_2O_8$ Ceramics with H_3BO_3 Addition. *J. Mater. Sci.: Mater. Electron.* **2016**, *27*, 6564−6569.

(23) Tang, B.; Fang, Z. X.; Li, H.; Liu, L.; Zhang, S. R. Microwave Dielectric Properties of H_3BO_3-doped $Ca_{0.61}La_{0.39}Al_{0.39}Ti_{0.61}O_3$ Ceramics. *J. Mater. Sci.: Mater. Electron.* **2015**, *26*, 300−306.

(24) Wu, H. T.; Guo, J. D.; Bi, J. X.; Mei, Q. J. Effect of H_3BO_3 Addition on the Sintering Behavior and Microwave Dielectric Properties of Wolframite-type $MgZrNb_2O_8$ Ceramics. *J. Alloys Compd.* **2016**, *661*, 535−540.

(25) Chen, G. H.; Xu, H. R.; Yuan, C. L. Microstructure and Microwave Dielectric Properties of $Li_2Ti_{1-x}(Zn_{1/3}Nb_{2/3})_xO_3$ Ceramics. *Ceram. Int.* **2013**, *39*, 4887−4892.

(26) Bian, J. J.; Zhang, X. H. Structural Evolution, Grain Growth Kinetics and Microwave Dielectric Properties of $Li_2Ti_{1-x}(Mg_{1/3}Nb_{2/3})_xO_3$. *J. Eur. Ceram. Soc.* **2018**, *38*, 599−604.

(27) Zhang, J.; Zuo, R. Low-temperature Fired Thermal-stable Li_2TiO_3−NiO Microwave Dielectric Ceramics. *J. Mater. Sci.: Mater. Electron.* **2016**, *27*, 7962−7968.

(28) Toby, B. H. EXPGUI, a Graphical User Interface for GSAS. *J. Appl. Crystallogr.* **2001**, *34*, 210−213.

(29) Dorrian, J. F.; Newnham, R. E. Refinement of the Structure of Li_2TiO_3. *Mater. Res. Bull.* **1969**, *4*, 179−183.
(30) Kordes, E. Die Steinsalzstruktur der Verbindung Li_2TiO_3 und ihre Mischkristallbildung mit MgO und $Li_2Fe_2O_4$. *Z. Krist.-Cryst Mater.* **1935**, *92*, 139−153.
(31) Baddour-Hadjean, R.; Pereira-Ramos, J. P. Raman Microspectrometry Applied to the Study of Electrode Materials for Lithium Batteries. *Chem. Rev.* **2010**, *110*, 1278−1319.
(32) Ding, Y.; Bian, J. Structural Evolution, Sintering Behavior and Microwave Dielectric Properties of $(1-x)Li_2TiO_3$+xLiF Ceramics. *Mater. Res. Bull.* **2013**, *48*, 2776−2781.
(33) Zhang, T.; Zuo, R.; Jian, Z. Structure, Microwave Dielectric Properties, and Low-Temperature Sintering of Acceptor/Donor Codoped $Li_2Ti_{1-x}(Al_{0.5}Nb_{0.5})_xO_3$ Ceramics. *J. Am. Ceram. Soc.* **2016**, *99*, 825−832.
(34) Shannon, R. D. Dielectric Polarizabilities of ions in Oxides and Fluorides. *J. Appl. Phys.* **1993**, *73*, 348−366.
(35) Ogawa, H.; Kan, A.; Ishihara, S.; Higashida, Y. Crystal Structure of Corundum Type $Mg_4(Nb_{2-x}Ta_x)O_9$ Microwave Dielectric Ceramics with Low Dielectric Loss. *J. Eur. Ceram. Soc.* **2003**, *23*, 2485−2488.
(36) Ogawa, H.; Taketani, H.; Kan, A.; Fujita, A.; Zouganelis, G. Evaluation of Electronic State of $Mg_4(Nb_{2-x}Sb_x)O_9$ Microwave Dielectric Ceramics by First Principle Calculation Method. *J. Eur. Ceram. Soc.* **2005**, *25*, 2859−2863.
(37) Zhang, Q. L.; Zou, D.; Yang, H. Microwave Dielectric Properties of $Ba_3Ti_{4-x}(Zn_{1/3}Nb_{2/3})_xNb_4O_{21}$ for Low Temperature Co-fired Ceramics. *J. Eur. Ceram. Soc.* **2011**, *31*, 265−272.
(38) Yang, H.; Zhang, S.; Yang, H.; Li, E. Usage of P−V−L Bond Theory in Studying the Structural/Property Regulation of Microwave Dielectric Ceramics: a Review. *Inorg. Chem. Front.* **2020**, *7*, 4711−4753.
(39) Bosman, A. J.; Havinga, E. E. Temperature Dependence of Dielectric Constants of Cubic Ionic Compounds. *Phys. Rev.* **1963**, *129*, 1593−1600.
(40) Lee, H. J.; Hong, K. S.; Kim, S. J.; Kim, I. T. Dielectric Properties of Mnb_2O_6 Compounds (where M = Ca, Mn, Co, Ni, or Zn). *Mater. Res. Bull.* **1997**, *32*, 847−855.
(41) Yoon, S. H.; Kim, D. W.; Cho, S. Y.; Hong, K. S. Investigation of the Relations Between Structure and Microwave Dielectric Properties of Divalent Metal Tungstate Compounds. *J. Eur. Ceram. Soc.* **2006**, *26*, 2051−2054.
(42) Guo, H. H.; Zhou, D.; Pang, L. X.; Qi, Z. M. Microwave Dielectric Properties of Low Firing Temperature Stable Scheelite Structured $(Ca,Bi)(Mo,V)O_4$ Solid Solution Ceramics for LTCC Applications. *J. Eur. Ceram. Soc.* **2019**, *39*, 2365−2373.
(43) Wu, Y.; Zhou, D.; Guo, J.; Pang, L. X. Microwave Dielectric Properties and Low Temperature Firing of $(1-x)Li_2Zn_3Ti_4O_{12}-xLi_2TiO_3$ $(0.2 \le x \le 0.8)$ Ceramics with B_2O_3−CuO Addition. *J. Mater. Sci.: Mater. Electron.* **2013**, *24*, 1505−1510.
(44) Guo, H. H.; Zhou, D.; Du, C.; Wang, P. J.; Liu, W. F.; Pang, L. X.; Wang, Q. P.; Su, J. Z.; Singh, C.; Trukhanov, S. Temperature Stable $Li_2Ti_{0.75}(Mg_{1/3}Nb_{2/3})_{0.25}O_3$-based Microwave Dielectric Ceramics with Low Sintering Temperature and Ultra-low Dielectric Loss for Dielectric Resonator Antenna Applications. *J. Mater. Chem. C* **2020**, *8*, 4690−4700.
(45) Zhou, D.; Wang, H.; Pang, L. X.; Yao, X.; Wu, X. G. Low Temperature Firing of $BiSbO_4$ Microwave Dielectric Ceramic with B_2O_3−CuO Addition. *J. Eur. Ceram. Soc.* **2009**, *29*, 1543−1546.
(46) Zhou, H.; Wang, H.; Ding, X.; Yao, X. Microwave Dielectric Properties of $3Li_2O-Nb_2O_5-3TiO_2$ Ceramics with $Li_2O-V_2O_5$ Additions. *J. Mater. Sci.: Mater. Electron.* **2009**, *20*, 39−43.
(47) Zuo, H.; Tang, X.; Guo, H.; Wang, Q.; Dai, C.; Zhang, H.; Su, H. Effects of $BaCu(B_2O_5)$ Addition on Microwave Dielectric Properties of Li_2TiO_3 Ceramics for LTCC Applications. *Ceram. Int.* **2017**, *43*, 13913−13917.
(48) Zeng, Q.; Li, W.; Shi, J. L.; Guo, J. K.; Chen, H.; Liu, M. L. Effect of B_2O_3 on the Sintering and Microwave Dielectric Properties of M-phase $LiNb_{0.6}Ti_{0.5}O_3$ Ceramics. *J. Eur. Ceram. Soc.* **2007**, *27*, 261−265.
(49) Borisevich, A. Y.; Davies, P. K. Effect of V_2O_5 Doping on the Sintering and Dielectric Properties of M-Phase $Li_{1+x-y}Nb_{1-x-3y}Ti_{x+4y}O_3$ Ceramics. *J. Am. Ceram. Soc.* **2004**, *87*, 1047−1052.
(50) Zhu, J. H.; Liu, J. Y.; Zeng, Y. Low Temperature Sintering and Microwave Dielectric Properties of $Li_2O-3ZnO-5TiO_2$ Ceramics Doped with V_2O_5. *J. Mater. Sci.: Mater. Electron.* **2018**, *29*, 14455−14461.
(51) Chen, X.; Zhou, H.; Fang, L.; Chu, D.; Li, C.; Guo, R.; Wang, H. Microwave Dielectric Properties and its Compatibility with Silver Electrode of $LiNb_{0.6}Ti_{0.5}O_3$ with B_2O_3 and CuO Additions. *J. Mater. Sci.: Mater. Electron.* **2011**, *22*, 371−375.
(52) Li, L.; Hong, W. B.; Yan, X. J.; Chen, X. M. Preparation and Microwave Dielectric Properties of B_2O_3 Bulk. *Int. J. Appl. Ceram. Technol.* **2019**, *16*, 2047−2052.
(53) Zhang, C.; Qiu, H.; Xiong, Z. X. Low-Temperature Sintering of $Ba_5(Nb_{1-x}V_x)_4O_{15}$ Ceramics with H_3BO_3. *Key Eng. Mater.* **2008**, *368-372*, 132−135.
(54) Xiang, H.; Li, C.; Jantunen, H.; Fang, L.; Hill, A. E. An Ultra-low Loss $CaMgGeO_4$ Microwave Dielectric Ceramic and its Chemical Compatibility with Silver Electrodes for LTCC Applications. *ACS Sustainable Chem. Eng.* **2018**, *6*, 6458−6466.
(55) Guo, H. H.; Zhou, D.; Liu, W. F.; Pang, L. X.; Wang, D. W.; Su, J. Z.; Qi, Z. M. Microwave Dielectric Properties of Temperature-stable Zircon-type $(Bi, Ce)VO_4$ Solid Solution Ceramics. *J. Am. Ceram. Soc.* **2019**, *103*, 423−431.
(56) Chen, G. H.; Chen, J. S.; Kang, X. L.; Luo, Y.; Feng, Q.; Yuan, C. L.; Yang, Y.; Yang, T. Structural and Microwave Dielectric Properties of New $CaTi_{1-x}(Al_{0.5}Nb_{0.5})_xO_3$ Thermally Stable Ceramics. *J. Alloys Compd.* **2016**, *675*, 301−305.
(57) Fang, L.; Su, C.; Zhou, H.; Wei, Z.; Zhang, H. Novel Low-Firing Microwave Dielectric Ceramic $LiCa_3MgV_3O_{12}$ with Low Dielectric Loss. *J. Am. Ceram. Soc.* **2013**, *96*, 688−690.
(58) Joseph, N.; Varghese, J.; Siponkoski, T.; Teirikangas, M.; Sebastian, M. T.; Jantunen, H. Glass-Free $CuMoO_4$ Ceramic with Excellent Dielectric and Thermal Properties for Ultralow Temperature Cofired Ceramic Applications. *ACS Sustainable Chem. Eng.* **2016**, *4*, 5632−5639.
(59) Jiang, X.; Li, C.; Su, C.; Wei, Z.; Fang, L. Low Temperature Firing and Microwave Dielectric Properties of $BaCaV_2O_7$ Ceramics. *Ceram. Int.* **2015**, *41*, 5172−5176.
(60) Chen, K.; Yuan, J.; Luo, X. Compact Dual-band Dual Circularly Polarised Annular-ring Patch Antenna for BeiDou Navigation Satellite System Application. *IET Microw. Antennas Propag.* **2017**, *11*, 1079−1085.
(61) Wang, X. Y.; Yang, G. M. Dual Frequency and Dual Circular Polarization Slot Antenna for BeiDou Navigation Satellite System Applications. *Microwave Opt. Technol. Lett.* **2014**, *56*, 2222−2225.
(62) Liang, Z. X.; Yang, D. C.; Wei, X. C.; Li, E. P. Dual-Band Dual Circularly Polarized Microstrip Antenna With Two Eccentric Rings and an Arc-Shaped Conducting Strip. *IEEE Antennas Wirel. Propag. Lett.* **2016**, *15*, 834−837.
(63) Li, J.; He, B.; Fang, J.; Zhang, A. Compact Dual-Band Proximity-Fed Circularly Polarized Patch Antenna for BDS Applications. *Frequenz* **2015**, *69*, 407−412.
(64) Lui, K. W.; Murphy, O. H.; Toumazou, C. A Wearable Wideband Circularly Polarized Textile Antenna for Effective Power Transmission on a Wirelessly-Powered Sensor Platform. *IEEE Trans. Antennas Propag.* **2013**, *61*, 3873−3876.
(65) Yang, S. L. S.; Kishk, A. A.; Lee, K. F. Wideband Circularly Polarized Antenna With L-Shaped Slot. *IEEE Trans. Antennas Propag.* **2008**, *56*, 1780−1783.
(66) Poffelie, L. A. Y.; Soh, P. J.; Yan, S.; Vandenbosch, G. A. High-Fidelity All-Textile UWB Antenna With Low Back Radiation for Off-Body WBAN Applications. *IEEE Trans. Antennas Propag.* **2016**, *64*, 757−760.

https://dx.doi.org/10.1021/acsami.0c18836
ACS Appl. Mater. Interfaces XXXX, XXX, XXX−XXX

(67) Zhou, Y.-D.; Jiao, Y.-C.; Weng, Z.-B.; Ni, T. A Novel Single-Fed Wide Dual-Band Circularly Polarized Dielectric Resonator Antenna. *IEEE Antennas Wirel. Propag. Lett.* **2016**, *15*, 930−933.
(68) Zhang, M.; Li, B.; Lv, X. Cross-Slot-Coupled Wide Dual-Band Circularly Polarized Rectangular Dielectric Resonator Antenna. *IEEE Antennas Wirel. Propag. Lett.* **2014**, *13*, 532−535.
(69) Bi, K.; Wang, X.; Hao, Y.; Lei, M.; Dong, G.; Zhou, J. Wideband Slot-coupled Dielectric Resonator-based Filter. *J. Alloys Compd.* **2019**, *785*, 1264−1269.

https://dx.doi.org/10.1021/acsami.0c18836
ACS Appl. Mater. Interfaces XXXX, XXX, XXX−XXX